

## **PAPER**

View Article Online



Cite this: Phys. Chem. Chem. Phys., 2024, 26, 10343

# Picosecond quantum-classical dynamics reveals that the coexistence of light-induced microbial and animal chromophore rotary motion modulates the isomerization quantum yield of heliorhodopsin†

Riccardo Palombo, pab Leonardo Barneschi, pa Laura Pedraza-González, pc Xuchun Yang<sup>b</sup> and Massimo Olivucci\*<sup>ab</sup>

Rhodopsins are light-responsive proteins forming two vast and evolutionary distinct superfamilies whose functions are invariably triggered by the photoisomerization of a single retinal chromophore. In 2018 a third widespread superfamily of rhodopsins called heliorhodopsins was discovered using functional metagenomics. Heliorhodopsins, with their markedly different structural features with respect to the animal and microbial superfamilies, offer an opportunity to study how evolution has manipulated the chromophore photoisomerization to achieve adaptation. One question is related to the mechanism of such a reaction and how it differs from that of animal and microbial rhodopsins. To address this question. we use hundreds of quantum-classical trajectories to simulate the spectroscopically documented picosecond light-induced dynamics of a heliorhodopsin from the archaea thermoplasmatales archaeon (TaHeR). We show that, consistently with the observations, the trajectories reveal two excited state decay channels. However, inconsistently with previous hypotheses, only one channel is associated with the -C13-C14- rotation of microbial rhodopsins while the second channel is characterized by the -C11-C12- rotation typical of animal rhodopsins. The fact that such -C11-C12- rotation is aborted upon decay and ground state relaxation, explains why illumination of TaHeR only produces the 13-cis isomer with a low quantum efficiency. We argue that the documented lack of regioselectivity in double-bond excited state twisting motion is the result of an "adaptation" that could be completely lost via specific residue substitutions modulating the steric hindrance experienced along the isomerization motion.

Received 16th January 2024, Accepted 11th March 2024

DOI: 10.1039/d4cp00193a

rsc.li/pccp

## Introduction

Rhodopsins are a class of transmembrane proteins constituted by a seven α-helices apoprotein (opsin) hosting a retinal protonated Schiff base chromophore (rPSB) covalently linked to a lysine residue. rPSB absorbs light and transduces it into nuclear motion leading to the breaking, isomerization and reconstitution of a specific C=C double-bond. The resulting rPSB isomer triggers the formation of opsin conformers that, ultimately, drive biological functions such as vision in

vertebrates; light-sensing, phototaxis, photoprotection, ionpumping in eubacteria and archaea; ion-gating in algae and catalytic activity in fungi, algae, and choanoflagellates, just to cite a few. 1-6 Such diverse functions emerge from the drastic differences in the protein amino acid sequence. The effect of such differences is already evident at the rPSB isomerization level that, in fact, displays different regioselectivity, stereoselectivity and quantum yield  $(\varphi_{iso})$  in different rhodopsins.<sup>7</sup> The study of the diversity of the rPSB isomerization and its efficiency is therefore an unavoidable milestone along the path to exploit rhodopsin functions. More specifically, it has become apparent that the investigation of the molecular-level factors controlling  $\varphi_{\mathrm{iso}}^{-8,9}$  in diverse rhodopsins would have an impact on the design of effective optogenetic tools 10,11 for neurosciences 12-14 and of novel synthetic biology circuits allowing, for instance, for artificial CO2 fixation. 15,16 Furthermore, the investigation of such factors is needed to understand how in photic zones such as the upper ocean, 17 specific microbial rhodopsins massively

a Dipartimento di Biotecnologie, Chimica e Farmacia, Università di Siena, via A. Moro 2, I-53100 Siena, Siena, Italy. E-mail: olivucci@unisi.it

<sup>&</sup>lt;sup>b</sup> Department of Chemistry, Bowling Green State University, Bowling Green, Ohio 43403, USA. E-mail: molivuc@bgsu.edu

<sup>&</sup>lt;sup>c</sup> Dipartimento di Chimica e Chimica Industriale, Università di Pisa, Via Giuseppe Moruzzi, 13, I-56124 Pisa, Italy

<sup>†</sup> Electronic supplementary information (ESI) available. See DOI: https://doi.org/ 10.1039/d4cp00193a

contribute to the solar energy capture.<sup>18</sup> Despite these facts, only a limited number of studies have targeted the rPSB isomerization diversity in both animal<sup>19–21</sup> and microbial<sup>22–27</sup> rhodopsins. For this reason, we present a computational study of the photoisomerization mechanism and dynamics of a member of a recently discovered rhodopsin family and compare the results to those obtained for the evolutionarily distant dim-light visual pigment of vertebrates.

The discovery of heliorhodopsins (HeRs) in Lake Tiberias (Israel), then readily detected in eubacteria, archaea, algae and viruses in both freshwater and saltwater environments worldwide, dramatically expanded the known rhodopsin diversity.<sup>28</sup> HeRs have an inverted membrane orientation topology exposing the C-terminus at the extracellular side, rather than the Nterminus as is the case for animal and microbial rhodopsin homologues. Furthermore, they share no more than 15% of sequence identity with both the former and the latter. Different HeR functions have been proposed. For instance, although the slow HeR photocycle could indicate a potential light sensory activity, 28,29 other novel metabolic functions such as light driven transport of amphiphilic molecules<sup>30</sup> and DNA protection against light-induced oxidative damage have been proposed.31 In addition, certain viral HeRs have been demonstrated to serve as proton channels, making them possible template for the development of optogenetic tools.<sup>32</sup> Finally, the growing interest on HeRs is also motivated by their possible exploitation as lightdriven redox enzymes possibly capable of carbon fixation.<sup>33</sup>

The first crystallographic structure of one representative of HeRs family, the thermoplasmatales archaeon heliorhodopsin (TaHeR), was released in 2019 under the PDB code 6IS6. 34 Like canonical microbial (or Type 1) rhodopsins, the TaHeR function was shown to be initiated by the all-trans to 13-cis photoisomerization of the rPSB chromophore occurring on a sub-picosecond timescale.35 This event triggers an internal proton transfer<sup>28</sup> event (i.e. the proton is never released from the protein) toward the counterion (Glu108) of the rPSB chromophore and then, according to a recent computational study<sup>36</sup> based on HeR 48C12 (43% of sequence identity with TaHeR), toward a nearby histidine pair, namely His23 and His80. The photoisomerization quantum yield  $(\varphi_{iso})$  does not exceed 0.20.35 Strikingly, this is a small value compared to 0.64 for the canonical proton-pump bacteriorhodopsin<sup>37</sup> as well as 0.67 for dim-light visual pigments.<sup>38</sup> While such differences point to a diverse photoisomerization mechanism in TaHeR and, possibly, in HeRs in general, it provides the opportunity to study how evolutionarily distant opsins modulate  $\varphi_{iso}$  and, therefore, an "elementary" chemical process such as the  $\pi$ -bond breaking.

Below we use quantum-classical population dynamics to study TaHeR. More specifically, we study the rPSB photoisomerization reaction by constructing, starting from the crystallographic structure, a hybrid multiconfigurational quantum mechanics/molecular mechanics (QM/MM) model of the protein and using it to propagate hundreds of Tully's quantum-classical trajectories<sup>39</sup> forover two picoseconds. The results are then compared with those of the rPSB photoisomerization reaction

occurring in the dim-light visual rhodopsin expressed in the vertebrate Bos taurus (Rh) as an example of highly efficient 11-*cis* to all-*trans* photoisomerization of a canonical animal (*i.e.* Type 2) rhodopsin.

We show that, while in Rh the rPSB photoisomerization is accomplished through a single coordinate describing the counterclockwise (CCW)  $\pi$ -bond breaking of the C11=C12 doublebond typical of animal rhodopsins, in TaHeR the isomerization motion follows simultaneously two coordinates corresponding to the clockwise (CW) and CCW  $\pi$ -bond breaking of the C13=C14 and C11=C12 double-bonds, respectively. This result has two consequences; firstly, it provides an atomistic reinterpretation of recent transient absorption spectroscopy (TAS) measurements, 35 which pointed to the existence of two ultrafast decay channels, but both assigned to C13=C14 isomerization. Secondly, it reveals a previously unreported and effective way in which HeRs control  $\varphi_{iso}$ . In fact, the same quantum-classical simulations, show that the absence of the C11=C12 isomerization product in TaHeR is explained by a ground state mechanism that selectively inverts the animal-like isomerization motion initiated in the excited state and leads to reconstitution of the original all-trans rPSB reactant.

## Results and discussion

Fig. 1 introduces the isomerization channels discussed for TaHeR and Rh in the following subsections. Light absorption promotes the rPSB in the all-trans (in TaHeR) or 11-cis (in Rh) configuration, from the ground electronic state (S<sub>0</sub>) to the Franck-Condon (FC) region of the first excited  $(S_1)$  state. The  $S_0 \rightarrow S_1$  change in electronic character induces an ultrafast relaxation that steers rPSB toward one or more S<sub>1</sub>/S<sub>0</sub> conical intersections (CoIn's) featuring a ca. 90° twisted double-bond. Each CoIn provides access to the S<sub>0</sub> potential energy surface (PES) and, ultimately, to photoproduct formation. The timescale of this process defines the S<sub>1</sub> lifetime while the branching along the isomerization coordinates associated with different skeletal C10-C11-C12-C13 and C12-C13-C14-C15 dihedral angles  $(\alpha, \alpha')$  in Fig. 1A and B) determines the isomerization regioselectivity. As we will discuss below, when compared to Rh that propagates exclusively along  $\alpha$ , TaHeR is non-regioselective since the S<sub>1</sub> population splits in a bifurcation region (BF in Fig. 1C) initiating parallel  $\alpha$ ,  $\alpha'$  propagations reaching the CoIn<sub>11</sub> and CoIn<sub>13</sub> channels, respectively. In Fig. 1B we also define  $\tau$ , a function of the skeletal torsion  $\alpha$  and substituents wag  $\beta$  proportional to the  $\pi$ -overlap of the isomerizing double bond. In the following,  $\tau$  is used to discuss the bond-breaking and bond-making process. As schematically shown in Fig. 1C, from each CoIn, two So relaxation paths can be accessed leading either to the photoproduct or to the reactant reconstitution. Thus, in TaHeR where only the C13=C14 isomerization product has been observed, the isomerization quantum efficiency  $(\varphi_{iso,13})$  must be a composite quantity that depends on both the S<sub>1</sub> population splitting at BF and the branching at CoIn<sub>13</sub>. The description of the "inversion mechanism"

selectively blocking the C11=C12 isomerization (see dashed curly red arrow in Fig. 1C, left) and explaining its observed negligible  $\phi_{iso,11}$ , is one of the main target of the present

research.

 $S_1$  lifetime, reaction regionelectivity,  $\varphi_{iso,13}$  and  $\varphi_{iso,11}$  of TaHeR and Rh are calculated by simulating their lightinduced dynamics starting from room-temperature So populations (details are provided in Sections S1 and S2, ESI†). Based on a recent study by some of us, we assume that 200 trajectories are suitable for mechanistic investigations as well as for comparative studies of diverse systems.9 The results are documented and discussed in Sections A-D. In A we validate the QM/MM models of TaHeR and Rh by comparing a set of calculated and experimentally observed spectral quantities. In B we report on the dramatically different time progression of the two corresponding photoexcited populations, showing that, in TaHeR, two structurally adjacent isomerization channels are equally populated. In C, we provide evidence indicating that stereochemically opposite aborted bicycle-pedal isomerization mechanisms characterize the two channels in TaHeR. Finally, in D, we rationalize the computed  $\varphi_{iso,13}$  and  $\varphi_{iso,11}$  values

using the theoretical framework based on functions of  $\tau$ : a parameter proportional to  $\pi$ -orbital overlap velocity of the reacting  $\pi$ -bond at the point of  $S_1$  decay  $(d\tau/dt^{decay})$ .

#### A. Absorption spectroscopy and model validation

The QM/MM models of TaHeR and Rh were constructed using the automatic rhodopsin modelling protocol, 40-43 a-ARM (see also Methods and Section S1, ESI†). A general overview of the two models is provided in Fig. 2A and B. The flexible part (in red) of the modelled chromophore cavities not only displays very different amino acidic compositions (see also Fig. S1, ESI†), but also a different three-dimensional shape. Notably, the cavity of TaHeR features a lateral fenestration visible above the β-ionone ring of the rPSB chromophore which exposes the chromophore itself to the external environment.<sup>34</sup> As shown in Fig. 2C and D, the constructed TaHeR and Rh models yielded FC vertical excitation energies (here expressed in terms of absorption maxima,  $\lambda_{\text{max}}^{\text{a}}$ ) only 12 nm blue shifted (530 nm) and 1 nm red shifted (499 nm) relative to the observed values, respectively. Furthermore, by using the wild-type QM/MM models as starting point for constructing a set of mutant models, 44 it was possible

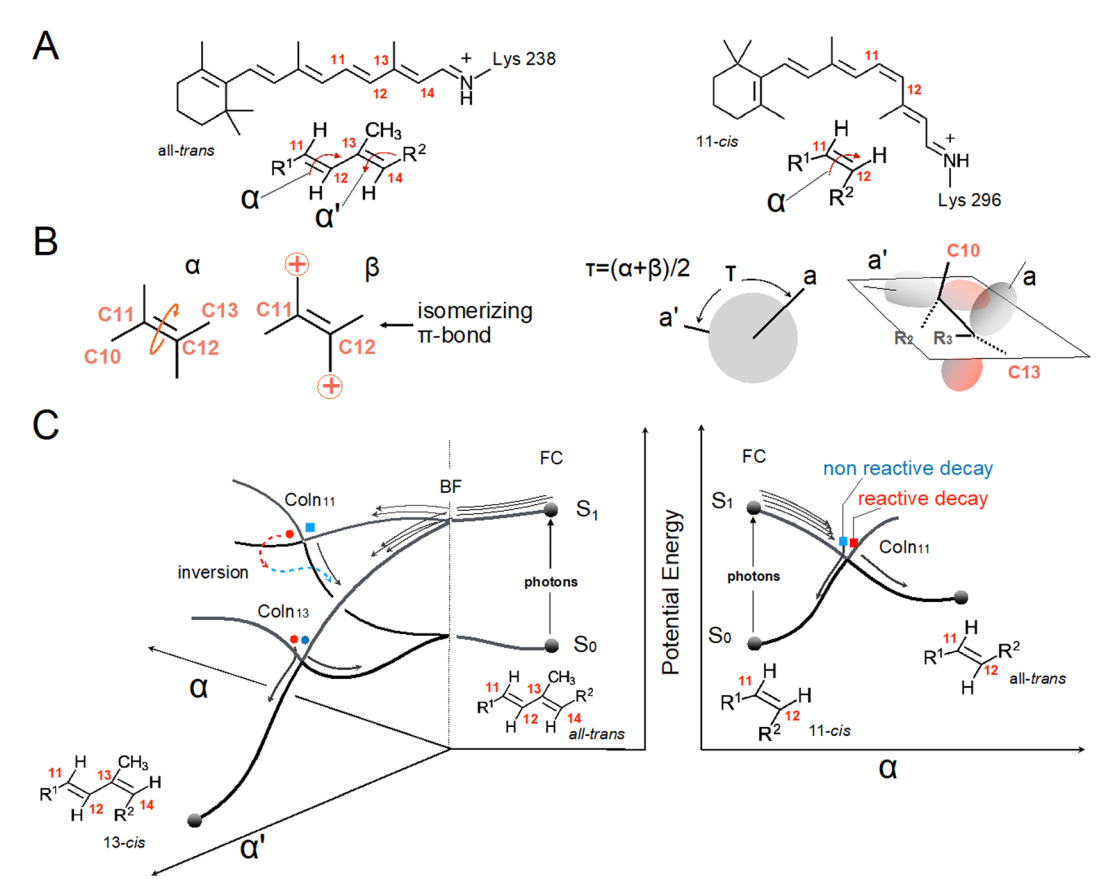


Fig. 1 S<sub>1</sub> isomerization channels in TaHeR and Rh. (A) Retinal chromophore in TaHeR (left) and Rh (right). The moiety at the bottom represents the reactive part of the two chromophores. The curly arrows indicate the  $S_1$  reaction coordinates of interest and  $\alpha$  and  $\alpha'$  represents the rotation (or torsional or twisting) about C11—C12 and C13—C14 respectively. (B) Schematic representation of  $\alpha$ ,  $\beta$  and  $\tau$ . The same representations apply to  $\alpha'$  and  $\beta'$  and the corresponding  $\tau'$  parameter.  $\tau$  and  $\tau'$  are geometrical parameters proportional to the  $\pi$ -overlap (roughly, the dihedral between the axes a and a' of the p-orbitals forming the  $\pi$ -bond) of the corresponding double bond. (C) Schematic representation of the photoisomerization channels in TaHeR (left) and Rh (right). The arrows in the FC region indicate the S<sub>1</sub> dynamics that, in TaHeR but not in Rh, leads to an ultrafast breaking (at BF) of the photoexcited population in two subpopulations reaching the regioselective CoIn<sub>11</sub> and CoIn<sub>13</sub> decay channels.

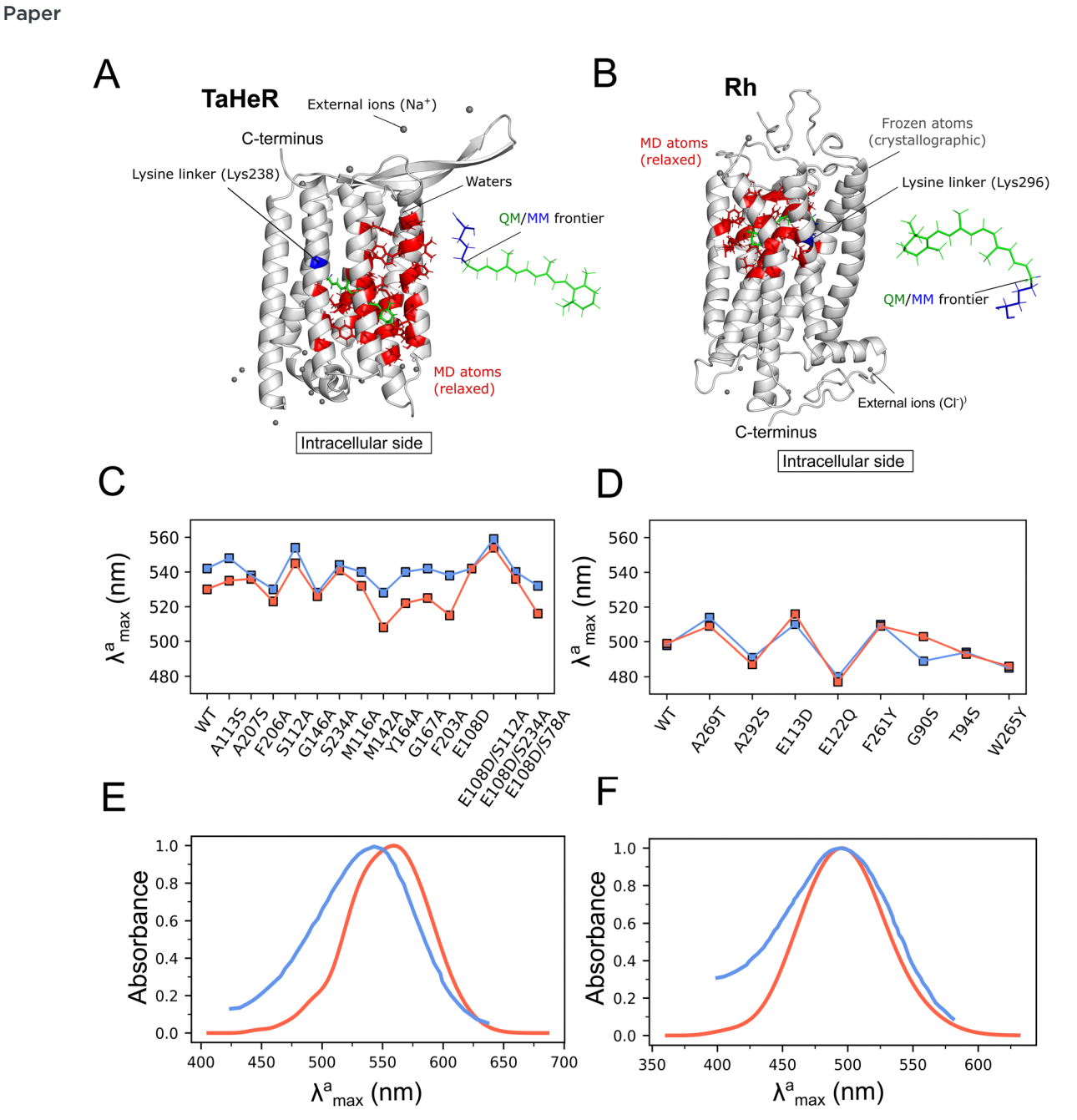


Fig. 2 TaHeR and Rh models validation. Overview of the QM/MM models for (A) TaHeR and (B) Rh. For each case, the protein environment fixed at the crystallographic position is colored in gray while the flexible binding cavity is in red. The lysine linker and rPSB chromohore are colored in blue and green respectively reflecting the QM/MM partition. Dark and light gray spheres indicate Na+ and Cl- external counterions, respectively. The intracellular side of the protein is marked to show how the C-terminus of TaHeR is oriented oppositely with respect to Rh. (C) Comparison between computed (in orange) and observed (in blue) absorption maxima wavelengths  $\lambda_{\max}^a$ , calculated as vertical excitation energies for a set of TaHeR mutants. (D) Same as point C for Rh mutants reported in ref. 42. (E) Comparison between computed (in orange) and observed (in blue) absorption bands (in arbitrary units) for TaHeR. (F) Same as point E for Rh. The experimental bands were digitalized from literature data. 34,47

to reproduce the trend in the observed  $\lambda^a_{max}$  displayed by a set of single mutants of Rh,41 and a set of single and double mutants of TaHeR (in most cases with a blue-shifted error typical of a-ARM models<sup>10,11,41,43-45</sup>). The glutamic-to-aspartic acid mutation at the 108 counterion position of TaHeR yielded identical  $\lambda_{max}^{a}$  value with respect to the wild-type, again in line with the observation.46 Also, it is worthwhile mentioning that in our TaHeR model the protonation state of the two peculiar His23 and His82 residues is consistent with the proposed proton release pathway (see Section S1.1, ESI†). The agreement between computed and observed spectral data supports the use of the QM/MM models for simulating the corresponding roomtemperature Boltzmann distributions and calculation of the absorption band. The computed absorption bands (see Fig. 2E and F) confirm the quality of the distribution represented by 200 geometries and velocities.

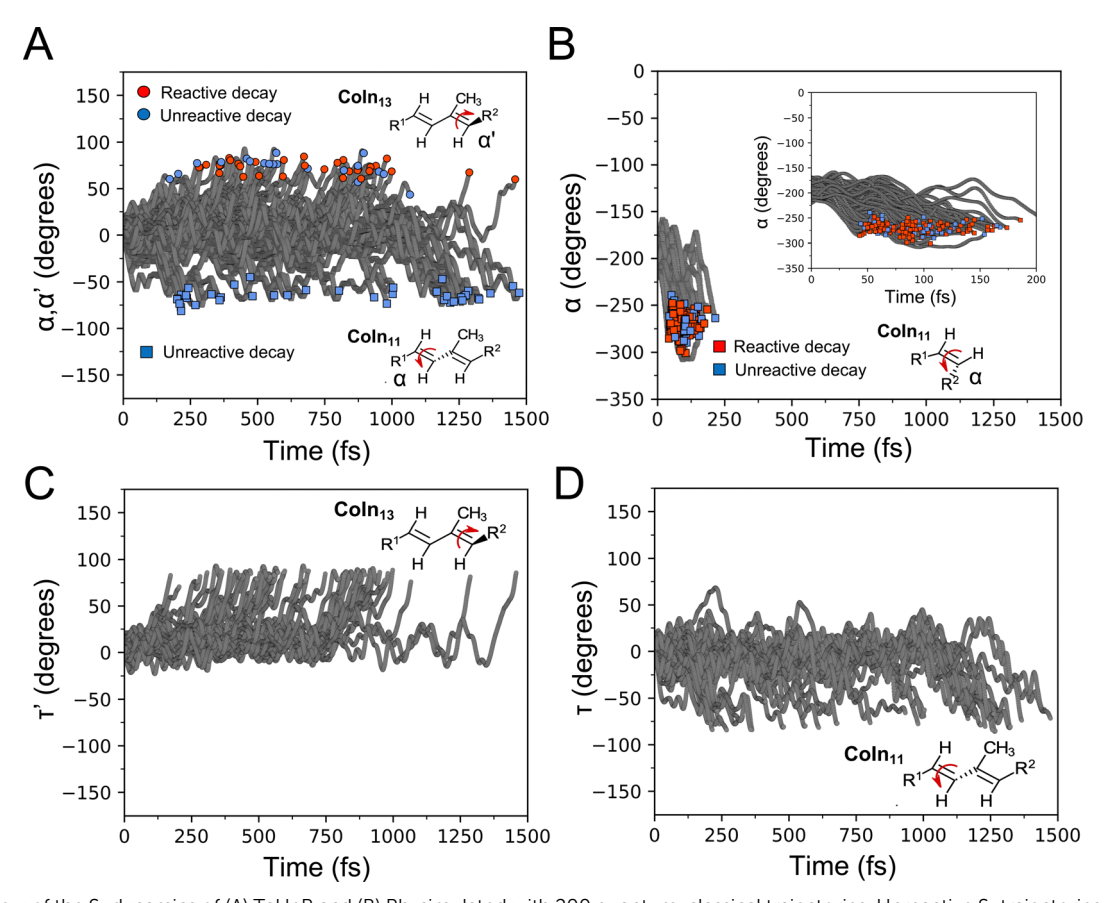


Fig. 3 Overview of the S<sub>1</sub> dynamics of (A) TaHeR and (B) Rh, simulated with 200 quantum-classical trajectories. Unreactive S<sub>1</sub> trajectories are marked by blue symbols placed at the time of the  $S_1 \rightarrow S_0$  decay (hopping time). Similarly, reactive trajectories are marked by red symbols. We termed as reactive the trajectory that, after the hopping, continue to propagate on So in the direction of the photoproduct. In contrast, unreactive trajectories revert their direction and propagate in the direction of the reactant (see also red and blue markers in Fig. 1C). In A, both  $\alpha$  and  $\alpha'$  coordinates (see Fig. 1A) are shown in order to illustrate the two coexisting isomerizations, however, a separate view is given in Fig. S5 (ESI†). (C) Evolution of the overlap index  $\tau'$  along the TaHeR trajectories undergoing C13=C14 isomerization (i.e. channel CoIn<sub>13</sub>) until the  $S_1 \rightarrow S_0$  decay point. (D) Same as C but for the index  $\tau$  associated to C11=C12 isomerization (i.e. channel Coln<sub>11</sub>).

#### Excited state dynamics and TAS assignment

The datasets representing the Boltzmann distribution of TaHeR and Rh (see above) are used as initial conditions for the propagation of 200 quantum-classical trajectories (see methods and Section S2 for details, ESI†). The room temperature geometries reveal a pre-twisting of the rPSB chromophore that is known<sup>7</sup> to bias the S<sub>1</sub> motion in the CW or CCW directions. In fact, the average structure obtained from the initial conditions shows, in TaHeR, an average +9° CW pre-twisting of the C13=C14 double bond while, in Rh, an average CCW twisting of  $-13^{\circ}$  of the C11=C12 double bond (these values are also consistent with those seen in the static a-ARM models of Fig. S3, ESI†).

The extreme difference in amino acid composition between Rh and TaHeR cavities (see Fig. S1, ESI†) is reflected in a qualitative, but drastic, different S<sub>1</sub> dynamics. This appears ballistic and substantially coherent in Rh but slower and more complex in TaHeR. This is shown in Fig. 3A and B where the time evolution of  $\alpha$  and  $\alpha'$  is displayed for each trajectory. By comparing the two figures, it becomes apparent that while the S<sub>1</sub> decay of TaHeR is not completed after 1.5 ps (only 93 out of 200 hopped to S<sub>0</sub>), Rh exhibits a full S<sub>1</sub> depopulation in less

than 0.2 ps (see also the different population decay profiles in Fig. S4, ESI†). This difference is already evident at <0.05 ps timescales, when most Rh trajectories exhibit a large CCW C11=C12 twist (ca. -70° on average) while no TaHeR double bond displays a twist larger than  $\pm 20^{\circ}$ . After this initial phase, all 200 Rh trajectories decay to So at a single CoIn11 channel and reconstitute the C11=C12  $\pi$ -bond in either the CW or the CCW directions. This does not occur in TaHeR where both CoIn<sub>11</sub> and CoIn<sub>13</sub> channels, featuring a distinct regiochemistry and stereochemistry, are populated and coexist for the entire simulation time. CoIn<sub>13</sub> (see red and blue circles in Fig. 3A respectively) is dominated by the CW twisting of the C13=C14 double bond. CoIn<sub>11</sub> (see blue squares in Fig. 3A), on the other hand, is dominated by the CCW twisting of the C11=C12 double bond, in full analogy with Rh. Notably, the two TaHeR competing channels yield nearly identical decay counts (52 and 41 decays, respectively, after 1.5 ps of simulation time).

With the purpose of further characterizing the population of the TaHeR channels, we computed the S<sub>1</sub> minimum energy paths (MEPs) connecting the Franck-Condon (FC) point to the minimum energy conical intersections associated to the CoIn<sub>11</sub>

and CoIn<sub>13</sub> paths (see Section S3 for details, ESI†). The results show that the two channels are achieved through reaction coordinates spanning very flat S<sub>1</sub> PES regions from -180° to  $-220^{\circ}$  along  $\alpha$  and from  $-170^{\circ}$  to  $-130^{\circ}$  along  $\alpha'$ . These MEPs are very different from the steep MEP reported for Rh<sup>48</sup> but consistent with the longer S<sub>1</sub> dynamics experimentally observed for TaHeR.<sup>35</sup> The analysis of the overlap coordinates  $\tau$  and  $\tau'$  in TaHeR indicates a C13=C14 and C11=C12 bond breaking process along a torsional or, as documented in the next section, bicycle-pedal coordinate that, in both cases, leads initially to an oscillatory C=C torsional motion in the  $-35^{\circ}$  to  $+35^{\circ}$  range then followed by a decay event (Fig. 3C and D). In other words, all TaHeR trajectories display a nearly planar (i.e. with a nearly  $0^{\circ}$ average torsion)  $\pi$ -system that, eventually, escapes such an oscillatory region along the two isomerization paths that are randomly accessed during the simulation time. Such random behaviour is further strengthened by the absence of any discernible correlation between early (<30 fs) geometrical motions and the two isomerization directions (see Fig. S7-S9, ESI†). Therefore, the S1 dynamics exhibited in the FC region (see Fig. 1C) seem to have a null or little impact on determining the isomerization direction.

In the past, flat S<sub>1</sub> PES have been proposed to be responsible for longer S<sub>1</sub> lifetimes of microbial rhodopsins with respect to Rh. 49,50 An alternative reason for the slow S<sub>1</sub> dynamics has been reported to be the mixing of the S<sub>1</sub> and S<sub>2</sub> states.<sup>9,51</sup> Indeed, compared to S<sub>1</sub> which is usually associated with a charge transfer state, S2 is associated with a diradical state featuring a shorter and semi-locked C=C double bonds. Thus, the mixing would be partly responsible for the increased excited state lifetime since isomerizations along these bonds became

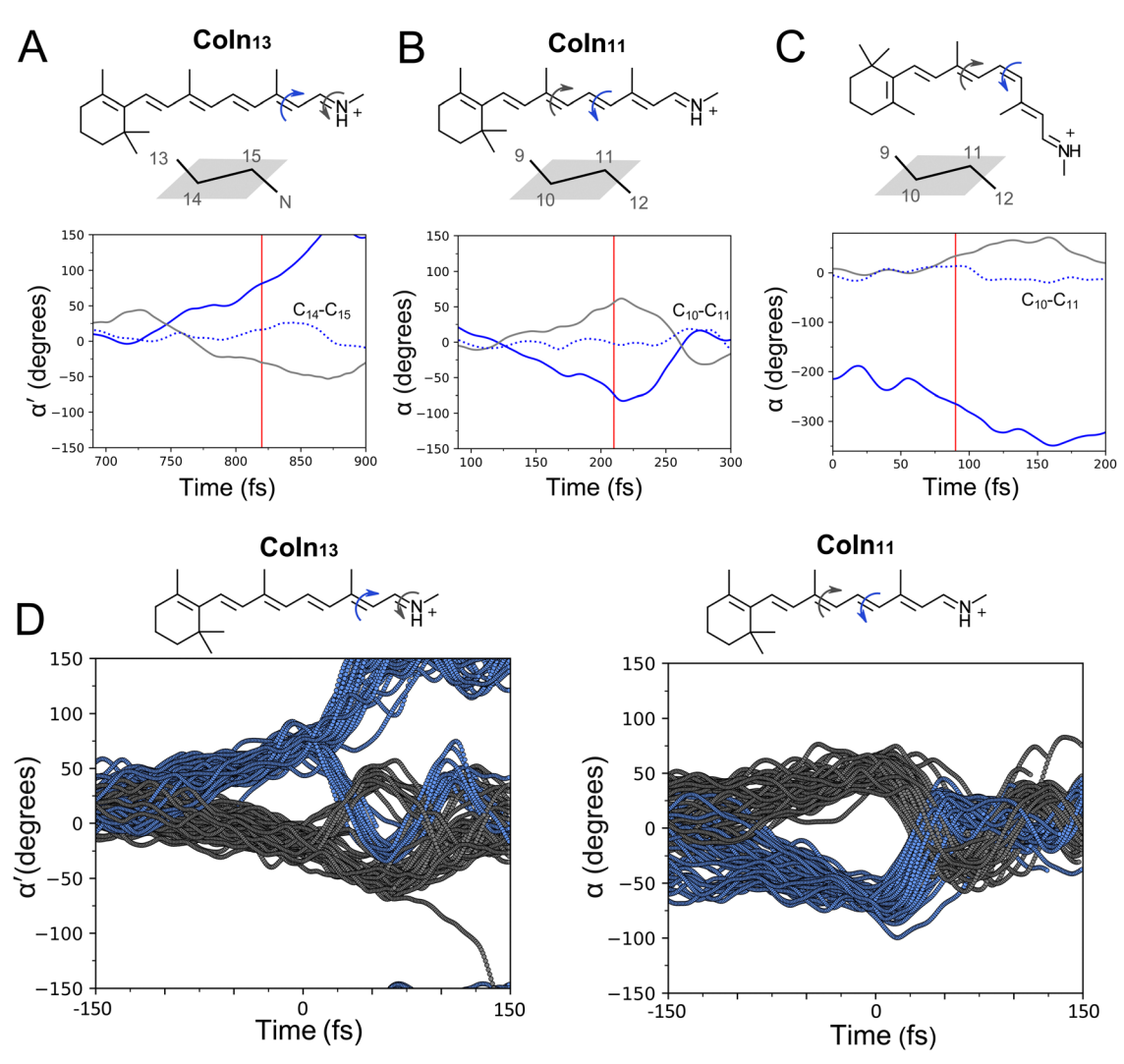


Fig. 4 Time evolution of the ABP photoisomerization coordinates of TaHeR and Rh. (A) A representative reactive trajectory achieving the CoIn<sub>13</sub> channel of TaHeR (coordinate  $\alpha'$  in Fig. 1), (B) a representative trajectory (unreactive) entering the Coln<sub>11</sub> channel of TaHeR (coordinate  $\alpha$  in Fig. 1). (C) A reactive Rh trajectory. The main torsional deformations (see blue and gray curly arrows) are represented in terms of rotating planes as illustrated at the top. In all cases, the diagrams reported on the geometrical changes consistent with the bicycle-pedal motion and rotating planes. The progression of the C13—C14-C15—N and C9—C10-C11—C12 dihedral angles is displayed as dotted lines. The vertical red lines correspond to  $S_1 \rightarrow S_0$  decay events. (D) Same representation of above but including instead all the trajectories achieving the Coln<sub>13</sub> (left panel) or the Coln<sub>11</sub> (right panel) channels of TaHeR. The trajectories were aligned at the  $S_1 \rightarrow S_0$  decay time (t = 0 fs). It is shown that while the CoIn<sub>13</sub> is partially reactive, the CoIn<sub>11</sub> is fully unreactive.

more impaired. As documented in the ESI† (see Section S4), the same level of S2/S1 mixing is detected in TaHeR trajectories leading to either the CoIn<sub>13</sub> or CoIn<sub>11</sub> channels and also the

trajectories that do not decayed to S<sub>0</sub> (see Fig. S10–S12, ESI†). The computed timescales are qualitatively consistent with the observed TAS dynamics for both TaHeR35 and Rh52 thus providing a further validation of the constructed QM/MM models. For TaHeR, TAS has shown that the  $S_1 \rightarrow S_0$  decay is completed after several ps (>8.5 ps) and exhibits a multiexponential decay including fast (<1 ps) and slow (>1 ps) components. More specifically, the presence of those components has been drawn from the time evolution of the stimulated emission (SE), ground state bleaching (GSB) and excited state absorption (ESA) temporal profiles, with the latter shown to be a valid and reliable indicator of the S<sub>1</sub> depopulation.<sup>53</sup> However, these observations were interpreted by assuming that the C13=C14 rotation is the sole excited state photoisomerization process. Therefore, the fast as well as slower components were associated to a multi-exponential process where the subpicosecond formation of the 13-cis photoproduct begins ca. 0.2 ps after photoexcitation, while slower decay components were attributed to "unreactive processes" generating less or no photoproduct. Our TaHeR simulation indicates that the observed fast and slower decay components are the result of the coexistence of the two S<sub>1</sub> isomerization channels described above. More specifically, our calculations associate the observed fast and slow decays of TaHeR with the presence of S<sub>1</sub> isomerizations with distinct dynamics, regioselectivity, stereoselectivity and efficiencies. Indeed, although in our trajectories (Fig. 3A) earlier decays are observed approximately after 0.2 ps, the majority of CoIn<sub>13</sub> decays take place within 1 ps (only 3 out of 52 trajectories decayed after 1 ps), while along CoIn<sub>11</sub> the trajectories decay more sparsely on a longer timescale. In striking contrast, the simulated Rh dynamics that fully complies with TAS measurements, 52,54 shows that the rPSB photoisomerization occurs, substantially, through a single mono-exponential decay (we disregard the very inefficient formation of isorhodopsin featuring a C9=C10 rotation<sup>55</sup>). Thus, in TaHeR the low  $\varphi_{iso,13}$  value would be the results of lack of isomerization regioselectivity during S<sub>1</sub> progression combined with an unreactive animal-like C11=C12 decay at CoIn<sub>11</sub>. In fact, the 41 trajectories decaying through the CoIn<sub>11</sub> channel, lead to reconstitution of the original all-trans rPSB exclusively (see blue squares, Fig. 3A). Conversely, the CoIn<sub>13</sub> channel is highly "reactive", as out of the 52 trajectories evolving along this path, 33 lead to photoproduct formation (see red circles, Fig. 3A) with 13-cis, 15-trans (32 trajectories) or 13-cis, 15-cis configurations (1 trajectory), as observed experimentally, 34 and the remaining 19 relax back to the all-trans rPSB configuration (see blue circles, Fig. 3A). Based on the assumption that the trajectories left on S<sub>1</sub> never decay productively (see above), we computed a 0.17  $\varphi_{iso,13}$  value (33 reactive trajectories over 200) of TaHeR, which is close to the experimentally observed  $\varphi_{iso}$ value of 0.19. Concerning Rh, all the trajectories displayed  $S_1 \rightarrow$ S<sub>0</sub> decays within ca. 0.1 ps (first 49 fs last 218 fs). The predicted  $\varphi_{\rm iso}$  value is of 0.70, again in line with the observed 0.67.<sup>38</sup>

Table 1 Summary of predicted (Pred.), computed (Comp.) and experimental (Exp.)  $\varphi_{\rm iso}$ . Number of reactive trajectories is also shown. Values in parenthesis indicate the percentage of trajectories over the total number of trajectories decaying along each decay channel. Pred.  $\varphi_{\rm iso}$  is calculated using the  $d\tau/dt^{decay}$  sign (or  $d\tau'/dt^{decay}$ ) as the index for predicting if a trajectory is reactive or unreactive (refer to main text for definition). Comp.  $\varphi_{\rm iso}$  is calculated over 200 trajectories. It is important to note that, in TaHeR, only 93 trajectories decayed to S<sub>0</sub> (along CoIn<sub>11</sub> or CoIn<sub>13</sub>) and we consider the trajectories remained in S<sub>1</sub> as unreactive. N.D. refers to "not detected"

	Reactive	$\mathrm{d} au/\mathrm{d}t^{\mathrm{decay}}$ or $\mathrm{d} au'/\mathrm{d}t^{\mathrm{decay}a}$	Pred. $\varphi_{\mathrm{iso}}$	Comp. $\varphi_{\mathrm{iso}}$	Exp. $\varphi_{iso}$
Rh, CoIn <sub>11</sub>	139 (70%)	148 (74%)	0.74	0.70	$0.67^{38}$ $0.19^{35}$
TaHeR, CoIn <sub>13</sub> TaHeR, CoIn <sub>11</sub>	33 (63%) 0 (0%)	39 (74%) 20 (49%)	$0.75 \\ 0.49$	0.17 0	0.19** N.D.

 $<sup>^</sup>a$  Number of Rh and TaHeR CoIn<sub>11</sub> trajectories with  ${\rm d}\tau/{\rm d}t^{\rm decay}<0$  and, for TaHeR CoIn<sub>13</sub>, with  ${\rm d}\tau'/{\rm d}t^{\rm decay}>0$ .

#### C. Conterclockwise vs. clockwise rotation and aborted bycicle-pedal

Fig. 4 displays the time evolution of critical dihedral angles. In TaHeR the CW isomerization of the C13=C14 bond is strongly coupled with the CCW rotation of the C15=N bond leading to the CoIn<sub>13</sub> channel (see Fig. 4A). In fact, the decay occurs when the dihedral angle at C13=C14 and C15=N bonds are +80° and  $-30^{\circ}$ , respectively. Notice that the dihedral angle associated with the middle C14-C15 single bond is minimally changed. The same description can be applied to the C11=C12 isomerization that is coupled to an opposite C9=C10 motion (see Fig. 4B where, at decay, the dihedrals associated to C9=C10 and C11=C12 feature a twist of  $+55^{\circ}$  and  $-73^{\circ}$ , respectively). The described motions of the C13=C14-C15=N and C9=C10-C11=C12 moieties is consistent with the bicycle pedal (BP) isomerization mechanism. The BP mechanism has been originally proposed as "space saving" motion by Warshel for Rh.<sup>56</sup> More recently, it has been predicted that such a Rh mechanism is instead aborted48 as one of the two adjacent double bonds of the C9=C10-C11=C12 moiety inverts its rotation direction at decay as here replicated in Fig. 4C. This aborted bicycle pedal (ABP) mechanism has also been found in microbial rhodopsins such as bacteriorhodopsin49 and Anabaena Sensory rhodopsin50 and similarly, in animal rhodopsins where the 11-cis C11=C12 bond isomerizes. 55,57,58 Recently, the existence of computationally predicted ABP has been supported via time-resolved XFEL studies on Rh59 and bacteriorhodopsin.60

Our results support the conservation of the ABP mechanism in the HeR family. This is clearly shown at the population level in Fig. 4D, left diagram, where the CCW motion around C15=N reverts its rotation at decay to So, then producing the isomerization at the C13=C14 exclusively. Notice, however, the presence of one trajectory that exhibits a full BP mechanism yielding the 13cis, 15-cis photoproduct. The right diagram is related to the CoIn<sub>11</sub> channel and demonstrates that, in contrast with CoIn<sub>13</sub>, both C9=C10 and C11=C12 rotations invert directions immediately after decay to S<sub>0</sub> such that no net isomerization takes place.

#### D. Regioselectivity and quantum efficiency modulation in TaHeR

In this section we look at the mechanism responsible for the experimentally observed C13=C14 selectivity (i.e. only the

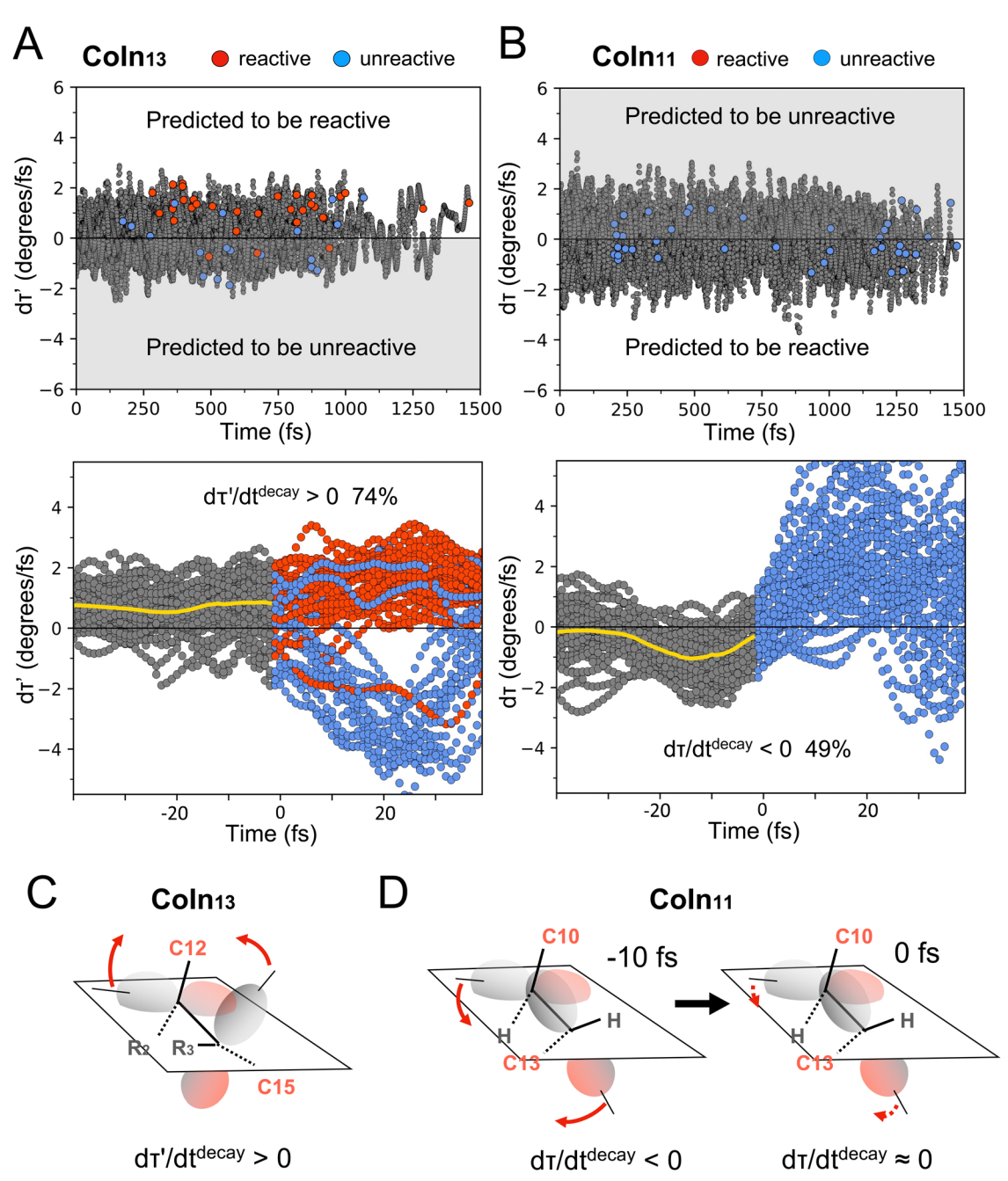


Fig. 5 Reactivity analysis of TaHeR trajectory sets. (A) Time evolution of the overlap index dr'/dt towards the CoIn<sub>13</sub> channel. The top panel shows the correlation between the distribution of reactive decays (red circles) and the dr'/dt sign. The bottom panel displays the same data but with trajectories aligned at the  $S_1 \rightarrow S_0$  decay time (t = 0 fs) and starting 40 fs before the decay. Gray data refers to the  $S_1$  while red and blue data refers to  $S_0$  depending on whether the trajectory is reactive (red) or unreactive (blue). The yellow curve represents the average value before the  $S_1 \rightarrow S_0$  decay. The displayed numerical value refers to the percentage of trajectories decaying with  $d\tau'/dt > 0$  (predicted quantum efficiency, see Table 1). To notice the behaviour of a few reactive and unreactive trajectories that do not correlate with, respectively, the  $d\tau'/dt > 0$  and  $d\tau'/dt < 0$  sign at the decay time. In these cases,  $d\tau'/dt$ inverts the sign after the decay point. These trajectories can be seen as those that deviate from the average behaviour but still falling in the expected statistics provided by the  $\tau$  velocity (see main text). (B) Same as A for the CCW motion leading to the CoIn<sub>11</sub> channel. Notice that now the displayed numerical value refers to  $d\tau/dt < 0$ . (C) Pictorial illustration of the  $\tau'$  velocity in terms of decreasing overlap along the CW progression towards the CoIn<sub>13</sub> channel. The curly arrow represents the rotational velocity of the orbital axes. (D) Same as C for the CoIn<sub>11</sub> channel where, in contrast, the velocity of the CCW overlap decrease is decelerating during the progression towards the decay channel.

C13=C14 isomerization is detected) and low  $\phi_{\mathrm{iso,13}}$  value of TaHeR in the presence of a non-regioselective S<sub>1</sub> isomerization dynamics. Past and recent studies on Rh<sup>8,9</sup> have demonstrated the pivotal role of the geometrical parameter  $\tau$  for the

mechanistic interpretation of reaction quantum efficiencies in Rh. More specifically, at decay one looks at the sign of the  $\tau$  velocity ( $d\tau/dt^{decay}$ ). Indeed, it has been established that in the CCW isomerization the  $d\tau/dt^{decay}$  < 0 provides a statistically

valid prediction of the corresponding computed  $\varphi_{iso,11}$  value. When considering the stereochemical change in rotation direction, in a CW isomerization such a prediction would be based in the fraction of trajectories decaying with  $d\tau/dt^{decay} > 0$ . These "rules" are connected and justified by the canonical Landau-Zener (LZ) model for a reactive non-adiabatic transition.61 In fact, the LZ model relates the probability of non-adiabatic transitions leading to the product (i.e. the probability that after S<sub>1</sub> decay the system would generate a product) to the nuclear velocity along the "local" reaction coordinate. A comparison of Fig. 5A and B demonstrates that such sign rule is valid for the C13=C14 isomerization (i.e. for decay through the CoIn<sub>13</sub> channel) of TaHeR but it is not valid for the C11=C12 isomerization (i.e. for decay through the CoIn<sub>11</sub> channel) in deep contrast with the reported validity in the case of the CoIn<sub>11</sub> channel of Rh. More specifically, in the top panel of Fig. 5A it can be seen that the vast majority of reactive trajectories (red circles) decay with  $d\tau'/dt^{decay} > 0$  (upper half of the panel). In deep contrast, Fig. 5B shows that irrespective of the sign of  $d\tau/dt^{\text{decay}}$  the trajectories are all unreactive.

The lower panels of Fig. 5A and B report an analysis of the  $d\tau/dt$  in the vicinity of the TaHeR decay regions. By focusing on a time window of 40 fs centered on the decay event, it is shown that  $\tau$  velocities behave differently along the paths leading to the two distinct channels. In the case of trajectories pointing to the CoIn<sub>13</sub> channel, the population displays a positive average velocity that appears to remain constant until the decay region is reached. This would translate into a constant velocity for the breaking of the  $\pi$ -bond as pictorially illustrated in Fig. 5C. In contrast, consistently with the illustration of Fig. 5D, the corresponding motion towards CoIn<sub>11</sub> displays decreasing τ velocities suggesting formation of the 11-cis product. However, about 10 fs before decay, a deceleration occurs, and the trajectories reach the decay region with rapidly decreasing velocities and yielding only small negative values at decay.

Fig. 5A and B also provide information on the TaHeR  $\pi$ -bond making dynamics immediately after the decay. It can be seen that, at CoIn<sub>13</sub>, the percentage of reactive trajectories generated at decay (63%) is relatively close to that of  $d\tau'/dt^{decay} > 0$  (74%). This does not happen in the case of the unreactive CoIn<sub>11</sub> channel (0%) where, despite a still large (49%) fraction of  $d\tau$ /  $\mathrm{d}t^{\mathrm{decay}} < 0$ ,  $\mathrm{d}\tau/\mathrm{d}t$  displays, immediately after the decay, large and positive values consistent with the resulting reactant reconstitution. This behavior suggests that in correspondence of the  $d\tau/dt$  decrease seen about 10 fs before the hopping points, the C11=C12 rotation or, better, the bicycle pedal

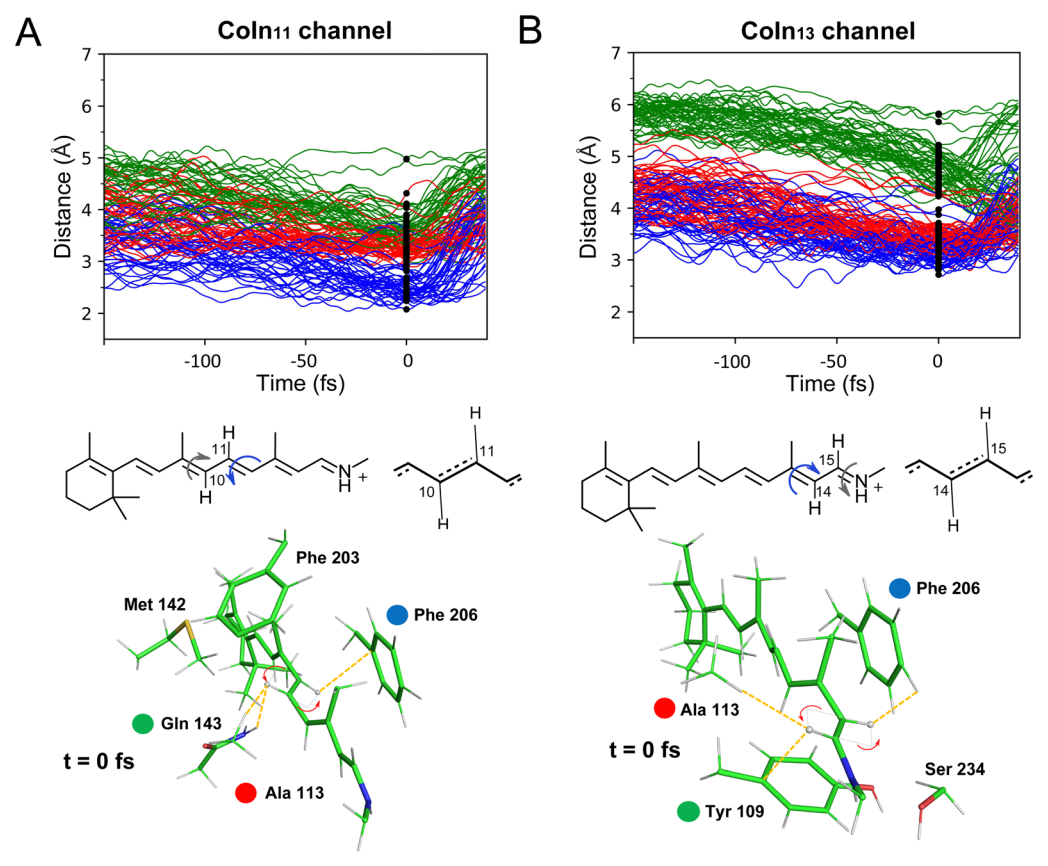


Fig. 6 Quantum efficiency quenching mechanism in TaHeR. (A) Population time evolution (trajectories aligned at the  $S_1 \rightarrow S_0$  decay time) of the shortest distances between the rPSB chromophore atoms characterizing the CW rotation of the bicycle-pedal plane of the Coln<sub>11</sub> channel with neighboring amino acids indicated below. The vertical set of black dots indicate the distribution of distances at the hopping points. Below, the definition and color coding of the distances monitored in the top. The rotating bicycle pedal plane is also defined pictorially and within a snapshot of the reacting rPSB region at the  $S_1 \rightarrow S_0$  decay time (t = 0 fs). (B) Same as A for the Coln<sub>13</sub> channel.

Paper

nuclear motion encounters a restraining force effectively inverting the motion from CCW to CW.

In order to provide a molecular-level understanding of the lack of reactivity of the CoIn<sub>11</sub> channel of TaHeR, we hypothesize that the restraining force mentioned above originate from steric and/or electrostatic interactions. Here the target is to provide a guidance to experimentalists that could eventually search for mutants capable of producing the 11-cis rPSB isomer. We start with the observation that the TaHeR cavity (see Fig. 6) accommodates the reactive C9=C10-C11=C12 moiety in the close vicinity of the Phe203, Phe206 and Tyr109 residues as well as of the polar Gln143 residue (Gln143 is absent in the cavities of most known microbial rhodopsins).34 Inspection of the TaHeR trajectories reveals that the C11=C12 rotation leads to strongly decreased distances between the plane associated with the BP coordinate and the listed residue sidechains (see Fig. 6A). This effect appears to lead to the "collision" of the rotation of the substituents at C10 and C11 with the  $\pi$ -system of Phe206 and the -NH2 aminic group of Gln143 causing compenetration of VdW radii<sup>62</sup> and, thus, strong repulsion. The same distance decrease may lead to electrostatic repulsion between the positive charged nitrogen of Gln143 amidic group and the chromophore positive charge that becomes increasingly localized on the -C9-C10-C11- moiety along the S<sub>1</sub> isomerization path (see last 50 fs of charge evolution in Fig. S10, ESI†). As anticipated above, these steric and electrostiatic effects may systematically invert the negative sign of  $d\tau/dt$  before and after the decay pointing to  $\pi$ -bond reconstitution via CW, rather than CCW, rotation. On the other hand, the rotation of the C13=C14-C15=N BP plane is less impaired (compare Fig. 6A with B), as demonstrated by the >2.5 Å distance kept by the C14 and C15 substituents with the closest residue sidechains during the progression toward the CoIn<sub>13</sub> channel.

Finally, as shown in Fig. S14 (ESI†), further analysis has been carried out to disentangle the importance of the steric vs. electrostatic repulsive effects. The figure shows that after switching the charges of the protein cavity to zero values, the "repulsive" effect documented above is conserved suggesting a steric origin of the repulsion.

## Conclusion

Above we have reported on the first atomistic description of the primary event in the photocycle of a member of the recently discovered HeR family. Since our TaHeR QM/MM model reproduces the observed spectroscopic parameters and measured  $\varphi_{iso}$ , we have use it to simulate the photoinduced dynamics and reinterpret the previously proposed mechanistic hypothesis.<sup>35</sup> The simulation reveals that TaHeR light absorption leads to an equal population of two regiochemically and stereochemically distinct S<sub>1</sub> isomerization channels. The first C13=C14 channel is found in substantially all microbial rhodopsins, while the second C11=C12 channel is related to the photoisomerization of animal rhodopsins but in the reversed all-trans to 11-cis direction. The coexistence of these two channels appears

connected with similar S<sub>1</sub> energy paths, which were found flat and substantially barrierless in both cases. These data may call TaHeR as promising candidate for isomerization selectivity control experiments. In fact, future studies may focus on the identification of variants that exhibit enhanced S1 isomerization energy barriers along one of the two channels. This could ultimately lead to a different branching ratio compared to the original (wild-type) system. Since TaHeR is phylogenetically distant from both animal and microbial rhodopsins, the resulting promiscuous photoisomerization provides and an example of a high isomerization diversity induced by diverse opsin cavity compositions. A second result is the finding of a new  $\varphi_{iso,13}$ modulation mechanism in TaHeR, not based on a low  $\varphi_{iso.13}$ but, rather, to the lack of S1 regioselectivity with respect to an equally populated fully inefficient C11=C12 S<sub>1</sub> isomerization channel. The suppression of the C11=C12 channel would allow, in principle, an increase of  $\phi_{\rm iso}$  from 0.17 to 0.63. A third result is the confirmation of the universality, i.e. its validity also for a HeRs member, of the space-saving ABP mechanism initially documented for Rh, 48 as well as of the validity of the theory based on  $\tau$ velocity at the point of  $S_1 \rightarrow S_0$  decay.<sup>8,9</sup>

Isomerization mechanisms featuring coexisting isomerization channels may operate in certain microbial rhodopsins. For instance, although the extreme distance between HeRs and microbial rhodopsins make any comparisons difficult, past and recent studies on chloride pump halorhodopsin, 63,64 proteorhodopsin, 23,65,66 sensory rhodopsin I (SRI),67 channelrhodopsin chimera C1C2,68 sodium ion pump rhodopsin KR269 as well as bacteriorhodopsin under acidic conditions,<sup>23</sup> have investigated the factors that govern their observed multicomponent excited state decay. Similarly to TaHeR, these microbial rhodopsins display an S1 dynamics well described by fast (subpicosecond) and reactive, and slow and unreactive decay components. Two types of mechanisms were proposed to rationalize the findings: (a) the potential heterogeneity of ground state species arising either from the acid-base equilibrium of the rPSB chromophore counterion or the presence of a mixture of chromophore isomers and (b) the possibility of reaction branching on S<sub>1</sub>. Our results support the latter mechanism in the case of TaHeR. In fact, for TaHeR, the presence of different chromophore isomers in the dark-adapted state can be excluded on the basis of HPLC measurements that document a dominant presence of all-trans rPSB. Furthermore, the TAS measurements are carried out at neutral pH that should ensure the deprotonation of the rPSB counterion (Glu108).<sup>35</sup>

A branched isomerization mechanism has been experimentally established for a microbial rhodopsin from Haloquadratum walsbyi called middle rhodopsin (MR)<sup>70</sup> where a mixture of 13-cis and 11-cis configurations is produced upon illumination starting from all-trans rPSB. It is possible that the isomerization mechanism of MR is essentially the same described above for TaHeR but having the all-trans to 11-cis isomerization channel corresponding to CoIn<sub>11</sub>, at least partially reactive. The authors of such research propose that MR might represent "a missing link" in the evolution from microbial to animal rhodopsins. It is apparent that the presented TaHeR investigation indicates

that such hypothesis could also apply to HeRs. More specifically, we envision that a mutation of the Gln143 causing a reduction in steric hindrance and/or reverting the dipole moment of this residue (i.e. pointing the positive -NH side of the dipole away from the isomerizing moiety) could make the two CoIn channels reactive providing a first example of HeRs variant capable of producing the 11-cis chromophore isomer typical of animal rhodopsins. Even more recently, the coexistence and interplay of C11=C12 and C13=C14 photoisomerizations was experimentally shown to be active in the rhodopsin tandem domains of the marine algae Phaeocystis antarctica bestrhodopsin.71

#### **Methods**

The computational models employed for bovine rhodopsin and thermoplasmatales archaeon rhodopsin were constructed with the a-ARM QM/MM model building protocol, 40,41 implemented in the PyARM software package, 11,42 starting from their crystallographic structures resolved at 2.4 Å (Protein Data Bank code: 1U19)<sup>72</sup> and 2.2 Å (Protein Data Bank code: 6IS6),<sup>34</sup> respectively. Such models were used to simulate two room temperature Boltzmann-like distributions and extract 200 initial conditions for each rhodopsin at room temperature following a previously reported protocol.9 Finally, non-adiabatic population dynamics were computed at 2 root (So and So) state average CASSCF(12,12)/6-31G\*/Amber94 level of theory using the stochastic Tully surfacehop method.<sup>39,73</sup> While the CASSCF method does not inherently incorporate dynamic correlation energy, benchmark studies<sup>74–77</sup> have demonstrated that the impact of the CASPT2 correction on these systems primarily affects the timescale rather than the geometrical propagation described by the trajectory itself. Therefore, we are confident that the mechanistic theory presented in this work would be replicated, at least qualitatively, in a study based on trajectories computed at the CASPT2 level. All the calculation were run using the Molcas version 8.178/Tinker79 interface. Further details of the a-ARM and initial condition protocols are provided in ESI† (Sections S1 and S2).

## Conflicts of interest

There are no conflicts to declare.

## Acknowledgements

M. O. is grateful to the NSF CHE-SDM A for Grant No. 2102619. R. P., L. B., X. Y. and M. O. are also grateful for partial support provided by EU funding within the MUR PNRR "National Center for Gene Therapy and Drugs based on RNA Technology" (Project no. CN00000041 CN3 RNA) - Spoke 6.

#### References

1 O. P. Ernst, D. T. Lodowski, M. Elstner, P. Hegemann, L. S. Brown and H. Kandori, Microbial and Animal

- Rhodopsins: Structures, Functions, and Molecular Mechanisms, Chem. Rev., 2014, 114(1), 126-163, DOI: 10.1021/ cr4003769.
- 2 H. Kandori, Retinal Proteins: Photochemistry and Optogenetics, Bull. Chem. Soc. Jpn., 2020, 93(1), 76-85, DOI: 10.1246/bcsj.20190292.
- 3 K.-H. Jung, V. D. Trivedi and J. L. Spudich, Demonstration of a Sensory Rhodopsin in Eubacteria, Mol. Microbiol., 2003, 47(6), 1513-1522, DOI: 10.1046/j.1365-2958.2003.03395.x.
- 4 G. Nagel, T. Szellas, W. Huhn, S. Kateriya, N. Adeishvili, P. Berthold, D. Ollig, P. Hegemann and E. Bamberg, Channelrhodopsin-2, a Directly Light-Gated Cation-Selective Membrane Channel, Proc. Natl. Acad. Sci. U. S. A., 2003, 100(24), 13940-13945, DOI: 10.1073/pnas.1936192100.
- 5 E. G. Govorunova, O. A. Sineshchekov, H. Li and J. L. Spudich, Microbial Rhodopsins: Diversity, Mechanisms, and Optogenetic Applications, Annu. Rev. Biochem., 2017, 86(1), 845-872, DOI: 10.1146/annurev-biochem-101910-144233.
- 6 A. Rozenberg, K. Inoue, H. Kandori and O. Béjà, Microbial Rhodopsins: The Last Two Decades, Annu. Rev. Microbiol., 2021, 75(1), 427-447, DOI: 10.1146/annurev-micro-031721-020452.
- 7 S. Gozem, H. L. Luk, I. Schapiro and M. Olivucci, Theory and Simulation of the Ultrafast Double-Bond Isomerization of Biological Chromophores, Chem. Rev., 2017, 117(22), 13502-13565, DOI: 10.1021/acs.chemrev.7b00177.
- 8 C. Schnedermann, X. Yang, M. Liebel, K. M. Spillane, J. Lugtenburg, I. Fernández, A. Valentini, I. Schapiro, M. Olivucci, P. Kukura and R. A. Mathies, Evidence for a Vibrational Phase-Dependent Isotope Effect on the Photochemistry of Vision, Nat. Chem., 2018, 10(4), 449-455, DOI: 10.1038/s41557-018-0014-y.
- 9 X. Yang, M. Manathunga, S. Gozem, J. Léonard, T. Andruniów and M. Olivucci, Quantum-Classical Simulations of Rhodopsin Reveal Excited-State Population Splitting and Its Effects on Quantum Efficiency, Nat. Chem., 2022, 14(4), 441-449, DOI: 10.1038/s41557-022-00892-6.
- 10 L. Barneschi, E. Marsili, L. Pedraza-González, D. Padula, L. De Vico, D. Kaliakin, A. Blanco-González, N. Ferré, M. Huix-Rotllant, M. Filatov and M. Olivucci, On the Fluorescence Enhancement of Arch Neuronal Optogenetic Reporters, Nat. Commun., 2022, 13(1), 6432, DOI: 10.1038/ s41467-022-33993-4.
- 11 L. Pedraza-González, L. Barneschi, M. Marszałek, D. Padula, L. De Vico and M. Olivucci, Automated QM/MM Screening of Rhodopsin Variants with Enhanced Fluorescence, J. Chem. Theory Comput., 2023, 19(1), 293-310, DOI: 10.1021/acs.jctc.2c00928.
- 12 E. S. Boyden, F. Zhang, E. Bamberg, G. Nagel and K. Deisseroth, Millisecond-Timescale, Genetically Targeted Optical Control of Neural Activity, Nat. Neurosci., 2005, 8(9), 1263-1268, DOI: 10.1038/nn1525.
- 13 F. Zhang, L.-P. Wang, M. Brauner, J. F. Liewald, K. Kay, N. Watzke, P. G. Wood, E. Bamberg, G. Nagel, A. Gottschalk and K. Deisseroth, Multimodal Fast Optical Interrogation of Neural Circuitry, Nature, 2007, 446(7136), 633-639, DOI: 10.1038/nature05744.

**Paper** 

14 K. Deisseroth and P. Hegemann, The Form and Function of Channelrhodopsin, *Science*, 2017, 357(6356), eaan5544, DOI: 10.1126/science.aan5544.

15 P. A. Davison, W. Tu, J. Xu, S. Della Valle, I. P. Thompson, C. N. Hunter and W. E. Huang, Engineering a Rhodopsin-Based Photo-Electrosynthetic System in Bacteria for CO<sub>2</sub> Fixation, ACS Synth. Biol., 2022, 11(11), 3805–3816, DOI: 10.1021/acssynbio.2c00397.

- 16 W. Tu, J. Xu, I. P. Thompson and W. E. Huang, Engineering Artificial Photosynthesis Based on Rhodopsin for CO<sub>2</sub> Fixation, *Nat. Commun.*, 2023, 14(1), 8012, DOI: 10.1038/s41467-023-43524-4.
- 17 O. Béjà, L. Aravind, E. V. Koonin, M. T. Suzuki, A. Hadd, L. P. Nguyen, S. B. Jovanovich, C. M. Gates, R. A. Feldman, J. L. Spudich, E. N. Spudich and E. F. DeLong, Bacterial Rhodopsin: Evidence for a New Type of Phototrophy in the Sea, *Science*, 2000, 289(5486), 1902–1906, DOI: 10.1126/science.289.5486.1902.
- 18 L. Gómez-Consarnau, J. A. Raven, N. M. Levine, L. S. Cutter, D. Wang, B. Seegers, J. Arístegui, J. A. Fuhrman, J. M. Gasol and S. A. Sañudo-Wilhelmy, Microbial Rhodopsins Are Major Contributors to the Solar Energy Captured in the Sea, *Sci. Adv.*, 2019, 5(8), eaaw8855, DOI: 10.1126/sciadv.aaw8855.
- 19 S. Inukai, K. Katayama, M. Koyanagi, A. Terakita and H. Kandori, Investigating the Mechanism of Photoisomerization in Jellyfish Rhodopsin with the Counterion at an Atypical Position, *J. Biol. Chem.*, 2023, **299**(6), 104726, DOI: **10.1016/j.jbc.2023.104726**.
- 20 M. M. T. El-Tahawy, A. Nenov, O. Weingart, M. Olivucci and M. Garavelli, Relationship between Excited State Lifetime and Isomerization Quantum Yield in Animal Rhodopsins: Beyond the One-Dimensional Landau–Zener Model, *J. Phys. Chem. Lett.*, 2018, 9(12), 3315–3322, DOI: 10.1021/ acs.jpclett.8b01062.
- 21 T. Mizukami, H. Kandori, Y. Shichida, A. H. Chen, F. Derguini, C. G. Caldwell, C. F. Biffe, K. Nakanishi and T. Yoshizawa, Photoisomerization Mechanism of the Rhodopsin Chromophore: Picosecond Photolysis of Pigment Containing 11-Cis-Locked Eight-Membered Ring Retinal, *Proc. Natl. Acad. Sci. U. S. A.*, 1993, 90(9), 4072–4076, DOI: 10.1073/pnas.90.9.4072.
- 22 K. Inoue, Photochemistry of the Retinal Chromophore in Microbial Rhodopsins, *J. Phys. Chem. B*, 2023, **127**(43), 9215–9222, DOI: **10.1021/acs.jpcb.3c05467**.
- 23 C. Chang, H. Kuramochi, M. Singh, R. Abe-Yoshizumi, T. Tsukuda, H. Kandori and T. Tahara, A Unified View on Varied Ultrafast Dynamics of the Primary Process in Microbial Rhodopsins, *Angew. Chem.*, *Int. Ed.*, 2022, 61(2), e202111930, DOI: 10.1002/anie.202111930.
- 24 R. Govindjee, S. P. Balashov and T. G. Ebrey, Quantum Efficiency of the Photochemical Cycle of Bacteriorhodopsin, *Biophys. J.*, 1990, **58**(3), 597–608, DOI: **10.1016/S0006-3495(90)82403-6**.
- 25 O. A. Smitienko, T. B. Feldman, L. E. Petrovskaya, O. V. Nekrasova, M. A. Yakovleva, I. V. Shelaev, F. E. Gostev, D. A. Cherepanov, I. B. Kolchugina, D. A. Dolgikh, V. A. Nadtochenko, M. P. Kirpichnikov and

- M. A. Ostrovsky, Comparative Femtosecond Spectroscopy of Primary Photoreactions of *Exiguobacterium Sibiricum* Rhodopsin and *Halobacterium Salinarum* Bacteriorhodopsin, *J. Phys. Chem. B*, 2021, 125(4), 995–1008, DOI: 10.1021/acs.jpcb.0c07763.
- 26 T. B. Feldman, O. A. Smitienko, I. V. Shelaev, F. E. Gostev, O. V. Nekrasova, D. A. Dolgikh, V. A. Nadtochenko, M. P. Kirpichnikov and M. A. Ostrovsky, Femtosecond Spectroscopic Study of Photochromic Reactions of Bacteriorhodopsin and Visual Rhodopsin, *J. Photochem. Photobiol., B*, 2016, 164, 296–305, DOI: 10.1016/j.jphotobiol.2016.09.041.
- 27 C.-F. Chang, M. Konno, K. Inoue and T. Tahara, Effects of the Unique Chromophore–Protein Interactions on the Primary Photoreaction of Schizorhodopsin, *J. Phys. Chem. Lett.*, 2023, 14(31), 7083–7091, DOI: 10.1021/acs.jpclett.3c01133.
- 28 A. Pushkarev, K. Inoue, S. Larom, J. Flores-Uribe, M. Singh, M. Konno, S. Tomida, S. Ito, R. Nakamura, S. P. Tsunoda, A. Philosof, I. Sharon, N. Yutin, E. V. Koonin, H. Kandori and O. Béjà, A Distinct Abundant Group of Microbial Rhodopsins Discovered Using Functional Metagenomics, *Nature*, 2018, 558(7711), 595–599, DOI: 10.1038/s41586-018-0225-9.
- 29 A. Shibukawa, K. Kojima, Y. Nakajima, Y. Nishimura, S. Yoshizawa and Y. Sudo, Photochemical Characterization of a New Heliorhodopsin from the Gram-negative Eubacterium *Bellilinea Caldifistulae* (BcHeR) and Comparison with Heliorhodopsin-48C12, *Biochemistry*, 2019, 58(26), 2934–2943, DOI: 10.1021/acs.biochem.9b00257.
- 30 J. Flores-Uribe, G. Hevroni, R. Ghai, A. Pushkarev, K. Inoue, H. Kandori and O. Béjà, Heliorhodopsins Are Absent in Diderm (Gram-negative) Bacteria: Some Thoughts and Possible Implications for Activity, *Environ. Microbiol. Rep.*, 2019, 11(3), 419–424, DOI: 10.1111/1758-2229.12730.
- 31 J. Shim, S.-G. Cho, S.-H. Kim, K. Chuon, S. Meas, A. Choi and K.-H. Jung, Heliorhodopsin Helps Photolyase to Enhance the DNA Repair Capacity, *Microbiol. Spectrosc.*, 2022, **10**(6), e02215–22, DOI: **10.1128/spectrum.02215-22**.
- 32 S. Hososhima, R. Mizutori, R. Abe-Yoshizumi, A. Rozenberg, S. Shigemura, A. Pushkarev, M. Konno, K. Katayama, K. Inoue, S. P. Tsunoda, O. Béjà and H. Kandori, Proton-Transporting Heliorhodopsins from Marine Giant Viruses, *eLife*, 2022, 11, DOI: 10.7554/eLife.78416.
- 33 K. Kovalev, D. Volkov, R. Astashkin, A. Alekseev, I. Gushchin, J. M. Haro-Moreno, I. Chizhov, S. Siletsky, M. Mamedov, A. Rogachev, T. Balandin, V. Borshchevskiy, A. Popov, G. Bourenkov, E. Bamberg, F. Rodriguez-Valera, G. Büldt and V. Gordeliy, High-Resolution Structural Insights into the Heliorhodopsin Family, *Proc. Natl. Acad. Sci. U. S. A.*, 2020, 117(8), 4131–4141, DOI: 10.1073/pnas.1915888117.
- 34 W. Shihoya, K. Inoue, M. Singh, M. Konno, S. Hososhima, K. Yamashita, K. Ikeda, A. Higuchi, T. Izume, S. Okazaki, M. Hashimoto, R. Mizutori, S. Tomida, Y. Yamauchi, R. Abe-Yoshizumi, K. Katayama, S. P. Tsunoda, M. Shibata, Y. Furutani, A. Pushkarev, O. Béjà, T. Uchihashi, H. Kandori and O. Nureki, Crystal Structure of

Heliorhodopsin, Nature, 2019, 574(7776), 132-136, DOI:

- 10.1038/s41586-019-1604-6.
- 35 S. Tahara, M. Singh, H. Kuramochi, W. Shihoya, K. Inoue, O. Nureki, O. Béjà, Y. Mizutani, H. Kandori and T. Tahara, Ultrafast Dynamics of Heliorhodopsins, J. Phys. Chem. B, 2019, 123(11), 2507-2512, DOI: 10.1021/acs.jpcb.9b00887.
- 36 M. Tsujimura, Y. Chiba, K. Saito and H. Ishikita, Proton Transfer and Conformational Changes along the Hydrogen Bond Network in Heliorhodopsin, Commun. Biol., 2022, 5(1), 1336, DOI: 10.1038/s42003-022-04311-x.
- 37 J. Tittor and D. Oesterhelt, The Quantum Yield of Bacteriorhodopsin, FEBS Lett., 1990, 263(2), 269-273, DOI: 10.1016/0014-5793(90)81390-A.
- 38 J. E. Kim, M. J. Tauber and R. A. Mathies, Wavelength Dependent Cis-Trans Isomerization in Vision, *Biochemistry*, 2001, 40(46), 13774-13778, DOI: 10.1021/bi0116137.
- 39 J. C. Tully, Molecular Dynamics with Electronic Transitions, J. Chem. Phys., 1990, 93(2), 1061-1071, DOI: 10.1063/1.459170.
- 40 F. Melaccio, M. del Carmen Marín, A. Valentini, F. Montisci, S. Rinaldi, M. Cherubini, X. Yang, Y. Kato, M. Stenrup, Y. Orozco-Gonzalez, N. Ferré, H. L. Luk, H. Kandori and M. Olivucci, Toward Automatic Rhodopsin Modeling as a Tool for High-Throughput Computational Photobiology, J. Chem. Theory Comput., 2016, 12(12), 6020-6034, DOI: 10.1021/acs.jctc.6b00367.
- 41 L. Pedraza-González, L. De Vico, M. Marín del C., F. Fanelli and M. Olivucci, a-ARM: Automatic Rhodopsin Modeling with Chromophore Cavity Generation, Ionization State Selection, and External Counterion Placement, J. Chem. Theory Comput., 2019, 15(5), 3134-3152, DOI: 10.1021/ acs.jctc.9b00061.
- 42 L. Pedraza-González, L. Barneschi, D. Padula, L. De Vico and M. Olivucci, Evolution of the Automatic Rhodopsin Modeling (ARM) Protocol, Top. Curr. Chem., 2022, 380(3), 21, DOI: 10.1007/s41061-022-00374-w.
- 43 L. Pedraza-González, M. D. C. Marín, A. N. Jorge, T. D. Ruck, X. Yang, A. Valentini, M. Olivucci and L. De Vico, Web-ARM: A Web-Based Interface for the Automatic Construction of QM/MM Models of Rhodopsins, J. Chem. Inf. Model., 2020, **60**(3), 1481–1493, DOI: 10.1021/acs.jcim.9b00615.
- 44 Y. Nakajima, L. Pedraza-González, L. Barneschi, K. Inoue, M. Olivucci and H. Kandori, Pro219 is an electrostatic color determinant in the light-driven sodium pump KR2, Commun. Biol., 2021, 4(1), 1185, DOI: 10.1038/s42003-021-02684-z.
- 45 R. Palombo, L. Barneschi, L. Pedraza-González, D. Padula, I. Schapiro and M. Olivucci, Retinal chromophore charge delocalization and confinement explain the extreme photophysics of Neorhodopsin, Nat. Commun., 2022, 13(1), 6652, DOI: 10.1038/s41467-022-33953-y.
- 46 T. Tanaka, M. Singh, W. Shihoya, K. Yamashita, H. Kandori and O. Nureki, Structural Basis for Unique Color Tuning Mechanism in Heliorhodopsin, Biochem. Biophys. Res. Commun., 2020, 533(3), 262-267, DOI: 10.1016/j.bbrc.2020.06.124.
- 47 H. Kandori, Y. Shichida and T. Yoshizawa, Photoisomerization in Rhodopsin, Biochemistry, 2001, 66(11), 1197-1209, DOI: 10.1023/A:1013123016803.

- 48 L. M. Frutos, T. Andruniów, F. Santoro, N. Ferré and M. Olivucci, Tracking the Excited-State Time Evolution of the Visual Pigment with Multiconfigurational Quantum Chemistry, Proc. Natl. Acad. Sci. U. S. A., 2007, 104(19), 7764-7769, DOI: 10.1073/pnas.0701732104.
- 49 P. Altoè, A. Cembran, M. Olivucci and M. Garavelli, Aborted Double Bicycle-Pedal Isomerization with Hydrogen Bond Breaking Is the Primary Event of Bacteriorhodopsin Proton Pumping, Proc. Natl. Acad. Sci. U. S. A., 2010, 107(47), 20172-20177, DOI: 10.1073/pnas.1007000107.
- 50 A. Strambi, B. Durbeej, N. Ferré and M. Olivucci, Anabaena Sensory Rhodopsin Is a Light-Driven Unidirectional Rotor, Proc. Natl. Acad. Sci. U. S. A., 2010, 107(50), 21322-21326, DOI: 10.1073/pnas.1015085107.
- 51 Y. Boeije and M. Olivucci, From a One-Mode to a Multi-Mode Understanding of Conical Intersection Mediated Ultrafast Organic Photochemical Reactions, Chem. Soc. Rev., 2023, 52(8), 2643–2687, DOI: 10.1039/D2CS00719C.
- 52 R. W. Schoenlein, L. A. Peteanu, R. A. Mathies and C. V. Shank, The First Step in Vision: Femtosecond Isomerization of Rhodopsin, Science, 1991, 254(5030), 412-415, DOI: 10.1126/science.1925597.
- 53 C. Xu, K. Lin, D. Hu, F. L. Gu, M. F. Gelin and Z. Lan, Ultrafast Internal Conversion Dynamics through the Onthe-Fly Simulation of Transient Absorption Pump-Probe Spectra with Different Electronic Structure Methods, J. Phys. Chem. Lett., 2022, 13(2), 661-668, DOI: 10.1021/ acs.jpclett.1c03373.
- 54 Q. Wang, R. W. Schoenlein, L. A. Peteanu, R. A. Mathies and C. V. Shank, Vibrationally Coherent Photochemistry in the Femtosecond Primary Event of Vision, Science, 1994, 266(5184), 422-424, DOI: 10.1126/science.7939680.
- 55 D. Polli, O. Weingart, D. Brida, E. Poli, M. Maiuri, K. M. Spillane, A. Bottoni, P. Kukura, R. A. Mathies, G. Cerullo and M. Garavelli, Wavepacket Splitting and Two-Pathway Deactivation in the Photoexcited Visual Pigment Isorhodopsin, Angew. Chem., Int. Ed., 2014, 53(9), 2504-2507, DOI: 10.1002/anie.201309867.
- 56 A. Warshel, Bicycle-Pedal Model for the First Step in the Vision Process, *Nature*, 1976, **260**(5553), 679–683, DOI: 10.1038/260679a0.
- 57 H. L. Luk, F. Melaccio, S. Rinaldi, S. Gozem and M. Olivucci, Molecular Bases for the Selection of the Chromophore of Animal Rhodopsins, Proc. Natl. Acad. Sci. U. S. A., 2015, 112(50), 15297-15302, DOI: 10.1073/pnas.1510262112.
- 58 S. Rinaldi, F. Melaccio, S. Gozem, F. Fanelli and M. Olivucci, Comparison of the Isomerization Mechanisms of Human Melanopsin and Invertebrate and Vertebrate Rhodopsins, Proc. Natl. Acad. Sci. U. S. A., 2014, 111(5), 1714-1719, DOI: 10.1073/pnas.1309508111.
- 59 M. Schmidt and E. A. Stojković, Earliest Molecular Events of Vision Revealed, Nature, 2023, 615(7954), 802-803, DOI: 10.1038/d41586-023-00504-4.
- 60 P. Nogly, T. Weinert, D. James, S. Carbajo, D. Ozerov, A. Furrer, D. Gashi, V. Borin, P. Skopintsev, K. Jaeger, K. Nass, P. Båth, R. Bosman, J. Koglin, M. Seaberg,

Paper

- T. Lane, D. Kekilli, S. Brünle, T. Tanaka, W. Wu, C. Milne, T. White, A. Barty, U. Weierstall, V. Panneels, E. Nango, S. Iwata, M. Hunter, I. Schapiro, G. Schertler, R. Neutze and I. Standfuss, Retinal isomerization in bacteriorhodopsin captured by a femtosecond X-ray laser, Science, 2018, 361(6398), DOI: 10.1126/science.aat0094.
- 61 C. Wittig, The Landau-Zener Formula, J. Phys. Chem. B, 2005, 109(17), 8428-8430, DOI: 10.1021/jp040627u.
- 62 S. S. Batsanov, van der Waals Radii of Elements, Inorg. Mater., 2001, 37(9), 871-885, DOI: 10.1023/A:1011625728803.
- 63 T. Arlt, S. Schmidt, W. Zinth, U. Haupts and D. Oesterhelt, The Initial Reaction Dynamics of the Light-Driven Chloride Pump Halorhodopsin, Chem. Phys. Lett., 1995, 241(5-6), 559-565, DOI: 10.1016/0009-2614(95)00664-P.
- 64 D. Oesterhelt, P. Hegemann and J. Tittor, The Photocycle of the Chloride Pump Halorhodopsin. II: Quantum Yields and a Kinetic Model, EMBO J., 1985, 4(9), 2351-2356, DOI: 10.1002/j.1460-2075.1985.tb03938.x.
- 65 M. O. Lenz, R. Huber, B. Schmidt, P. Gilch, R. Kalmbach, M. Engelhard and J. Wachtveitl, First Steps of Retinal Photoisomerization in Proteorhodopsin, Biophys. J., 2006, 91(1), 255-262, DOI: 10.1529/biophysj.105.074690.
- 66 K. Neumann, M.-K. Verhoefen, I. Weber, C. Glaubitz and J. Wachtveitl, Initial Reaction Dynamics of Proteorhodopsin Observed by Femtosecond Infrared and Visible Spectroscopy, Biophys. J., 2008, 94(12), 4796-4807, DOI: 10.1529/ biophysj.107.125484.
- 67 Y. Sudo, M. Mizuno, Z. Wei, S. Takeuchi, T. Tahara and Y. Mizutani, The Early Steps in the Photocycle of a Photosensor Protein Sensory Rhodopsin I from Salinibacter Ruber, J. Phys. Chem. B, 2014, 118(6), 1510-1518, DOI: 10.1021/jp4112662.
- 68 Y. Hontani, M. Marazzi, K. Stehfest, T. Mathes, I. H. M. van Stokkum, M. Elstner, P. Hegemann and J. T. M. Kennis, Reaction Dynamics of the Chimeric Channelrhodopsin C1C2, Sci. Rep., 2017, 7(1), 7217, DOI: 10.1038/s41598-017-07363-w.
- 69 S. Tahara, S. Takeuchi, R. Abe-Yoshizumi, K. Inoue, H. Ohtani, H. Kandori and T. Tahara, Origin of the Reactive and Nonreactive Excited States in the Primary Reaction of Rhodopsins: PH Dependence of Femtosecond Absorption of Light-Driven Sodium Ion Pump Rhodopsin KR2, J. Phys. Chem. B, 2018, 122(18), 4784-4792, DOI: 10.1021/ acs.jpcb.8b01934.
- 70 Y. Sudo, K. Ihara, S. Kobayashi, D. Suzuki, H. Irieda, T. Kikukawa, H. Kandori and M. Homma, A Microbial Rhodopsin with a Unique Retinal Composition Shows Both Sensory Rhodopsin II and Bacteriorhodopsin-like Properties, J. Biol. Chem., 2011, 286(8), 5967-5976, DOI: 10.1074/ jbc.M110.190058.
- 71 S. Kaziannis, M. Broser, I. H. M. van Stokkum, J. Dostal, W. Busse, A. Munhoven, C. Bernardo, M. Kloz, P. Hegemann

- and J. T. M. Kennis, Multiple retinal isomerizations during the early phase of the bestrhodopsin photoreaction, Proc. Natl. Acad. Sci. U. S. A., 2024, 121(12), e2318996121, DOI: 10.1073/pnas.2318996121.
- 72 T. Okada, M. Sugihara, A.-N. Bondar, M. Elstner, P. Entel and V. Buss, The Retinal Conformation and Its Environment in Rhodopsin in Light of a New 2.2 Å Crystal Structure, I. Mol. Biol., 2004, 342(2), 571-583, DOI: 10.1016/ j.jmb.2004.07.044.
- 73 G. Granucci and M. Persico, Critical Appraisal of the Fewest Switches Algorithm for Surface Hopping, J. Chem. Phys., 2007, 126(13), 134114, DOI: 10.1063/1.2715585.
- 74 S. Gozem, M. Huntress, I. Schapiro, R. Lindh, A. A. Granovsky, C. Angeli and M. Olivucci, Dynamic Electron Correlation Effects on the Ground State Potential Energy Surface of a Retinal Chromophore Model, J. Chem. Theory Comput., 2012, 8(11), 4069-4080, DOI: 10.1021/ ct3003139.
- 75 L. Barneschi, D. Kaliakin, M. Huix-Rotllant, N. Ferré, M. Filatov(Gulak) and M. Olivucci, Assessment of the Electron Correlation Treatment on the Quantum-Classical Dynamics of Retinal Protonated Schiff Base Models: XMS-CASPT2, RMS-CASPT2, and REKS Methods, J. Chem. Theory Comput., 2023, **19**(22), 8189–8200, DOI: **10.1021**/ acs.jctc.3c00879.
- 76 S. Sen and I. Schapiro, A Comprehensive Benchmark of the XMS-CASPT2 Method for the Photochemistry of a Retinal Chromophore Model, Mol. Phys., 2018, 116(19–20), 2571-2582, DOI: 10.1080/00268976.2018.1501112.
- 77 S. Gozem, M. Huntress, I. Schapiro, R. Lindh, A. A. Granovsky, C. Angeli and M. Olivucci, Dynamic Electron Correlation Effects on the Ground State Potential Energy Surface of a Retinal Chromophore Model, J. Chem. Theory Comput., 2012, 8(11), 4069-4080, DOI: 10.1021/ ct3003139.
- 78 F. Aquilante, J. Autschbach, R. K. Carlson, L. F. Chibotaru, M. G. Delcey, L. De Vico, I. F. Galván, N. Ferré, L. M. Frutos, L. Gagliardi, M. Garavelli, A. Giussani, C. E. Hoyer, G. Li Manni, H. Lischka, D. Ma, P. Å. Malmqvist, T. Müller, A. Nenov, M. Olivucci, T. B. Pedersen, D. Peng, F. Plasser, B. Pritchard, M. Reiher, I. Rivalta, I. Schapiro, J. Segarra-Martí, M. Stenrup, D. G. Truhlar, L. Ungur, A. Valentini, S. Vancoillie, V. Veryazov, V. P. Vysotskiy, O. Weingart, F. Zapata and R. Lindh, MOLCAS 8: New Capabilities for Multiconfigurational Quantum Chemical Calculations across the Periodic Table, J. Comput. Chem., 2016, 37(5), 506-541, DOI: 10.1002/jcc.24221.
- 79 J. A. Rackers, Z. Wang, C. Lu, M. L. Laury, L. Lagardère, M. J. Schnieders, J.-P. Piquemal, P. Ren and J. W. Ponder, Tinker 8: Software Tools for Molecular Design, J. Chem. Theory Comput., 2018, 14(10), 5273-5289, DOI: 10.1021/ acs.jctc.8b00529.